INTERNATIONAL JOURNAL FOR NUMERICAL METHODS IN FLUIDS
Int. J. Numer. Meth. Fluids **31**: 747–765 (1999)

IMPLICIT WEIGHTED ESSENTIALLY NON-OSCILLATORY SCHEMES FOR THE INCOMPRESSIBLE NAVIER–STOKES EQUATIONS

YIH-NAN CHEN[a], SHIH-CHANG YANG[a] AND JAW-YEN YANG[b,]*

[a] *Department of Mechanical Engineering, National Taiwan University, Taipei, Taiwan, Republic of China*
[b] *Institute of Applied Mechanics, National Taiwan University, Taipei, Taiwan, Republic of China*

SUMMARY

A class of lower–upper/approximate factorization (LUAF) implicit weighted essentially non-oscillatory (ENO; WENO) schemes for solving the two-dimensional incompressible Navier–Stokes equations in a generalized co-ordinate system is presented. The algorithm is based on the artificial compressibility formulation, and symmetric Gauss–Seidel relaxation is used for computing steady state solutions while symmetric successive overrelaxation is used for treating time-dependent flows. WENO spatial operators are employed for inviscid fluxes and central differencing for viscous fluxes. Internal and external viscous flow test problems are presented to verify the numerical schemes. The use of a WENO spatial operator not only enhances the accuracy of solutions but also improves the convergence rate for the steady state computation as compared with using the ENO counterpart. It is found that the present solutions compare well with exact solutions, experimental data and other numerical results. Copyright © 1999 John Wiley & Sons, Ltd.

KEY WORDS: WENO schemes; artificial compressibility; incompressible; Navier–Stokes equations

1. INTRODUCTION

The design and construction of the weighted essentially non-oscillatory (WENO) schemes for hyperbolic conservation laws are based on essentially non-oscillatory (ENO) schemes that were first introduced by Harten *et al.* [1] in the form of cell averages. Later, to improve the implementation of the method, Shu and Osher [2,3] devised a class of flux-based efficient ENO schemes. The main concept of ENO schemes is to use the 'smoothest' stencil (in the asymptotic sense) among several candidates to approximate the fluxes at cell boundaries to a high-order accuracy, and at the same time, to avoid oscillations near discontinuities. ENO schemes are uniformly high-order accurate right up to the shock and are very robust to use. However, they also have certain drawbacks as Jiang and Shu [4] have pointed out. One problem is that the freely adaptive stencil could change even by a round-off perturbation near zeroes of the solution and its derivatives. This free adaptation of the stencil is also not necessary in regions where the solution is smooth. The convergence rate for the implicit ENO scheme is generally poor. Another problem is that ENO schemes are not effective on vector supercomputers because the stencil-choosing step involves heavy usage of logical statement, which performs

---

* Correspondence to: Institute of Applied Mechanics, College of Engineering, National Taiwan University, Taipei 10764, Taiwan, Republic of China.

CCC 0271–2091/99/200747–19$17.50

Received August 1997
Revised July 1998

poorly on such machines. The WENO schemes proposed recently by Jiang and Shu [4] and by Liu *et al.* [5] can overcome these drawbacks while keeping the robustness and high-order accuracy of ENO schemes. The concept of WENO schemes is the following: instead of approximating the numerical flux using only one of the candidate stencils, one uses a convex combination of all the candidate stencils. Each of the candidate stencils is assigned a weight which determines the contribution of this stencil to the final approximation of the numerical flux. The weights are defined in such a way that, in smooth regions, it approaches certain optimal weights to achieve a higher order of accuracy, while in regions near discontinuities, the stencils that contain the discontinuities are assigned a nearly zero weight. Thus, ENO property is achieved by emulating ENO schemes around discontinuities and a higher order of accuracy is obtained by emulating upstream central schemes with the optimal weights away from the discontinuities. Both efficient ENO and WENO schemes have been extensively tested and applied to the compressible Euler/Navier–Stokes equations.

The solution methodology for viscous incompressible flows is rather different from that for compressible flows, due to the fact that there exists no time derivative in the continuity equation for incompressible flows. In order to apply compressible flow solution algorithms to incompressible flow problems, the continuity equation needs to be modified to couple with the momentum equation so that the whole system of equations can be put into the same formulation and solved efficiently. To achieve this goal, the artificial compressibility may be introduced by adding the time derivative of pressure to the continuity equation, as was first proposed by Chorin [6]. The modified continuity equation, together with the unsteady momentum equations, yield a set of hyperbolic–parabolic type of time-dependent system of equations. Thus, fast implicit schemes developed for compressible flows, such as the approximate-factorization scheme by Beam and Warming [7], can be implemented. Various applications that evolved from this artificial compressibility concept have been reported for obtaining steady state solutions [8–14]. Merkle and Athavale [15] and Rogers and Kwak [16,17] have reported successful computations using the pseudo-time iteration approach for the time-dependent flow problems. Further developments of numerical methods for incompressible viscous flows can be found in the work by Anderson *et al.* [18] and by Briley *et al.* [19].

In this paper, the WENO scheme of Jiang and Shu [4] is adopted and is extended to solve the incompressible flow problems. An implicit code of the WENO scheme is developed for the artificial compressibility formulation of the two-dimensional incompressible Navier–Stokes equations for both steady state and time-dependent flows. For the steady state flow problems, the lower–upper symmetric-Gauss–Seidel (LU-SGS) implicit algorithm [20] is adopted. This algorithm is not only unconditionally stable but also completely vectorizable in any dimension. For the time-dependent flow problems, the lower–upper symmetric successive overrelaxation (LU-SSOR) scheme [21] is employed. For saving CPU time, the pseudo-time iteration approach was not used. Instead, the values of β have been put in the range $\beta \geq 5$ (i.e. the larger the β value, the minor the influence of the time derivative term in the continuity equation becomes). The resulting schemes are applied to compute several standard internal and external laminar flow problems, including driven square cavity flow, flow over a backward-facing step, flow decayed by viscosity and flow over a circular cylinder. It is found that the present solutions are in good agreement with available experimental results, exact solutions and other numerical results.

2. GOVERNING EQUATIONS

The Navier–Stokes equations in the integral conservation law form for an incompressible, two-dimensional flow with artificial compressibility can be written as

$$\frac{\partial}{\partial t}\left(\frac{1}{\mathbf{V}}\int_{\mathbf{V}}\mathbf{Q}\,\mathrm{d}\mathbf{V}\right)+\frac{1}{\mathbf{V}}\oint_{\mathbf{S}}\vec{\mathbf{F}}\cdot\mathrm{d}\vec{\mathbf{S}}=0, \tag{1}$$

where $\mathbf{V}$ is the volume of the arbitrary control volume, $\mathbf{S}$ is the area of the arbitrary control surface and the direction of $\mathrm{d}\vec{\mathbf{S}}$ is outward, $\mathbf{Q}$ is the vector form of the conservative variables and $\vec{\mathbf{F}}=(\mathbf{E}-\mathbf{E}_v)\vec{i}+(\mathbf{F}-\mathbf{F}_v)\vec{j}$ is the flux tensor. In a Cartesian co-ordinates system, Equation (1) can be expressed as follows:

$$\frac{\partial\mathbf{Q}}{\partial t}+\frac{\partial(\mathbf{E}-\mathbf{E}_v)}{\partial x}+\frac{\partial(\mathbf{F}-\mathbf{F}_v)}{\partial y}=0, \tag{2}$$

with

$$\mathbf{Q}=\begin{bmatrix}p\\u\\v\end{bmatrix},\qquad \mathbf{E}=\begin{bmatrix}\beta u\\u^2+p\\uv\end{bmatrix},\qquad \mathbf{F}=\begin{bmatrix}\beta v\\vu\\v^2+p\end{bmatrix},$$

$$\mathbf{E}_v=Re^{-1}\begin{bmatrix}0\\2u_x\\u_y+v_x\end{bmatrix},\quad \mathbf{F}_v=Re^{-1}\begin{bmatrix}0\\v_x+u_y\\2v_y\end{bmatrix},$$

where β is the artificial compressibility parameter and $Re=\rho V_\infty L/\mu$ is the Reynolds number. The Cartesian velocity components u and v are scaled with the freestream velocity V_∞ and the Cartesian co-ordinates x and y are normalized with the characteristic length L. The non-dimensional pressure is defined as $p=(P-P_\infty)/\rho V_\infty^2$, and the dynamic viscosity μ is assumed to be constant.

Conventionally, Equation (2) is transformed into the generalized co-ordinates (ξ,η) as

$$\frac{\partial\hat{\mathbf{Q}}}{\partial t}+\frac{\partial(\hat{\mathbf{E}}-\hat{\mathbf{E}}_v)}{\partial\xi}+\frac{\partial(\hat{\mathbf{F}}-\hat{\mathbf{F}}_v)}{\partial\eta}=0, \tag{3}$$

where

$$\hat{\mathbf{Q}}=h\begin{bmatrix}p\\u\\v\end{bmatrix},\qquad \hat{\mathbf{E}}=h\begin{bmatrix}\beta U\\uU+\xi_x p\\vU+\xi_y p\end{bmatrix},\qquad \hat{\mathbf{F}}=h\begin{bmatrix}\beta V\\uV+\eta_x p\\vV+\eta_y p\end{bmatrix},$$

$$\hat{\mathbf{E}}_v=h[\xi_x\mathbf{E}_v+\xi_y\mathbf{F}_v],\qquad \hat{\mathbf{F}}_v=h[\eta_x\mathbf{E}_v+\eta_y\mathbf{F}_v]$$

and

$$U=\xi_x u+\xi_y v,\qquad V=\eta_x u+\eta_y v,\qquad h=\begin{vmatrix}x_\xi & x_\eta\\ y_\xi & y_\eta\end{vmatrix}=x_\xi y_\eta-x_\eta y_\xi.$$

3. NUMERICAL METHOD

3.1. Spatial discretization

A semi-discrete finite volume method is used to ensure that the final converged solution is independent of the integration procedure and to avoid metric singularity problems. The finite volume method is based on the local flux balance of each mesh cell. The semi-discrete form of Equation (3) can be written as

$$\begin{aligned}\frac{\partial \hat{\mathbf{Q}}}{\partial t} &= -\frac{1}{\mathbf{V}_{i,j}}\{[(\tilde{\mathbf{E}}-\tilde{\mathbf{E}}_v)\mathbf{S}]_{i+1/2,j}-[(\tilde{\mathbf{E}}-\tilde{\mathbf{E}}_v)\mathbf{S}]_{i-1/2,j}\}\\ &\quad -\frac{1}{\mathbf{V}_{i,j}}\{[(\tilde{\mathbf{F}}-\tilde{\mathbf{F}}_v)\mathbf{S}]_{i,j+1/2}-[(\tilde{\mathbf{F}}-\tilde{\mathbf{F}}_v)\mathbf{S}]_{i,j-1/2}\},\end{aligned} \tag{4}$$

where (i,j) is the (i,j)th computational cell with volume $\mathbf{V}_{i,j}$ and $\mathbf{S}$ is the area of each control surface and the direction is outward. The spatial differencing adopts fifth-order-accurate ($r=3$) WENO scheme (WENO3) [4] for the inviscid convective fluxes ($\hat{\mathbf{E}}$, $\hat{\mathbf{F}}$) and fourth-order central differencing for the viscous fluxes ($\hat{\mathbf{E}}_v$, $\hat{\mathbf{F}}_v$).

When adopting the WENO3 scheme, the physical fluxes (say $\hat{\mathbf{F}}$) are split locally into positive and negative parts as

$$\hat{\mathbf{F}}(\hat{\mathbf{Q}})=\hat{\mathbf{F}}^{+}(\hat{\mathbf{Q}})+\hat{\mathbf{F}}^{-}(\hat{\mathbf{Q}}), \tag{5}$$

where $\partial\hat{\mathbf{F}}^{+}/\partial\hat{\mathbf{Q}}\geq 0$ and $\partial\hat{\mathbf{F}}^{-}/\partial\hat{\mathbf{Q}}\leq 0$. There are several flux splitting methods that can be chosen. In this paper, the local Lax–Friedrichs flux splitting method is used

$$\hat{\mathbf{F}}^{\pm}(\hat{\mathbf{Q}})=\frac{1}{2}(\hat{\mathbf{F}}(\hat{\mathbf{Q}})\pm|\Lambda|\hat{\mathbf{Q}}), \tag{6}$$

where $|\Lambda|=\mathrm{diag}(|\lambda_1|, |\lambda_2|, |\lambda_3|)$ and λ_1, λ_2 and λ_3 are the local eigenvalues. For easy understanding, consider first the one-dimensional scalar conservation laws. For example,

$$u_t+f(u)_x=0. \tag{7}$$

Let us discretize the space into uniform intervals of size Δx and denote $x_j=j\Delta x$. Various quantities at x_j will be identified by the subscript j. The spatial operator of the WENO3 scheme that approximates $-f(u)_x$ at x_j will take the conservative form

$$\mathscr{L}=\frac{1}{\Delta x}(\tilde{f}_{j+1/2}-\tilde{f}_{j-1/2}), \tag{8}$$

where $\tilde{f}_{j+1/2}$ and $\tilde{f}_{j-1/2}$ are the numerical fluxes. If the numerical fluxes obtained from the positive and negative parts of $f(u)$ are designated $\tilde{f}^{+}_{j+1/2}$ and $\tilde{f}^{-}_{j+1/2}$ respectively, then we have

$$\tilde{f}_{j+1/2}=\tilde{f}^{+}_{j+1/2}+\tilde{f}^{-}_{j+1/2}. \tag{9}$$

Here we first describe the approximation of the numerical flux $\tilde{f}_{j+1/2}$ in one-dimensional scalar conservation law. The WENO3 numerical flux for the positive part of $f(u)$ is

$$\begin{aligned}\tilde{f}^{+}_{j+1/2} &= \omega_0^{+}\left(\frac{2}{6}f^{+}_{j-2}-\frac{7}{6}f^{+}_{j-1}+\frac{11}{6}f^{+}_{j}\right)+\omega_1^{+}\left(-\frac{1}{6}f^{+}_{j-1}+\frac{5}{6}f^{+}_{j}+\frac{2}{6}f^{+}_{j+1}\right)\\ &\quad+\omega_2^{+}\left(\frac{2}{6}f^{+}_{j}+\frac{5}{6}f^{+}_{j+1}-\frac{1}{6}f^{+}_{j+2}\right),\end{aligned} \tag{10}$$

where

$$\omega_k^+ = \frac{\alpha_k^+}{\alpha_0^+ + \alpha_1^+ + \alpha_2^+}, \quad k = 0, 1, 2,$$

$$\alpha_0^+ = \frac{1}{10}(\epsilon + \mathrm{IS}_0^+)^{-2}, \qquad \alpha_1^+ = \frac{6}{10}(\epsilon + \mathrm{IS}_1^+)^{-2}, \qquad \alpha_2^+ = \frac{3}{10}(\epsilon + \mathrm{IS}_2^+)^{-2},$$

$$\epsilon = 10^{-6},$$

and

$$\mathrm{IS}_0^+ = \frac{13}{12}(f_{j-2}^+ - 2f_{j-1}^+ + f_j^+)^2 + \frac{1}{4}(f_{j-2}^+ - 4f_{j-1}^+ + 3f_j^+)^2,$$

$$\mathrm{IS}_1^+ = \frac{13}{12}(f_{j-1}^+ - 2f_j^+ + f_{j+1}^+)^2 + \frac{1}{4}(f_{j-1}^+ - f_{j+1}^+)^2,$$

$$\mathrm{IS}_2^+ = \frac{13}{12}(f_j^+ - 2f_{j+1}^+ + f_{j+2}^+)^2 + \frac{1}{4}(3f_j^+ - 4f_{j+1}^+ + f_{j+2}^+)^2.$$

Similarly, the WENO3 numerical flux for the negative part of $f(u)$ is

$$\tilde{f}_{j+1/2}^- = \omega_0^-\left(-\frac{1}{6}f_{j-1}^- + \frac{5}{6}f_j^- + \frac{2}{6}f_{j+1}^-\right) + \omega_1^-\left(\frac{2}{6}f_j^- + \frac{5}{6}f_{j+1}^- - \frac{1}{6}f_{j+2}^-\right) + \omega_2^-\left(\frac{11}{6}f_{j+1}^- - \frac{7}{6}f_{j+2}^- + \frac{2}{6}f_{j+3}^-\right), \tag{11}$$

where

$$\omega_k^- = \frac{\alpha_k^-}{\alpha_0^- + \alpha_1^- + \alpha_2^-}, \quad k = 0, 1, 2,$$

$$\alpha_0^- = \frac{3}{10}(\epsilon + \mathrm{IS}_0^-)^{-2}, \qquad \alpha_1^- = \frac{6}{10}(\epsilon + \mathrm{IS}_1^-)^{-2}, \qquad \alpha_2^- = \frac{1}{10}(\epsilon + IS_2^-)^{-2},$$

$$\epsilon = 10^{-6},$$

and

$$\mathrm{IS}_0^- = \frac{13}{12}(f_{j-1}^- - 2f_j^- + f_{j+1}^-)^2 + \frac{1}{4}(f_{j-1}^- - 4f_j^- + 3f_{j+1}^-)^2,$$

$$\mathrm{IS}_1^- = \frac{13}{12}(f_j^- - 2f_{j+1}^- + f_{j+2}^-)^2 + \frac{1}{4}(f_j^- - f_{j+2}^-)^2,$$

$$\mathrm{IS}_2^- = \frac{13}{12}(f_{j+1}^- - 2f_{j+2}^- + f_{j+3}^-)^2 + \frac{1}{4}(f_{j+1}^- - 4f_{j+2}^- + f_{j+3}^-)^2.$$

Next the system of two-dimensional incompressible Navier–Stokes equations is considered, where the numerical flux $\tilde{\mathbf{F}}_{j+1/2}$ is usually approximated in the local characteristic fields. Let the Jacobian matrices $\hat{\mathbf{A}}$ and $\hat{\mathbf{B}}$ ($\hat{\mathbf{A}} = \partial\hat{\mathbf{E}}/\partial\hat{\mathbf{Q}}$, $\hat{\mathbf{B}} = \partial\hat{\mathbf{F}}/\partial\hat{\mathbf{Q}}$) be represented by the following:

$$\hat{\mathbf{A}}_i = \begin{bmatrix} 0 & k_x\beta & k_y\beta \\ k_x & \Theta + k_x u & k_y u \\ k_y & k_x v & \Theta + k_y v \end{bmatrix}, \tag{12}$$

where $\hat{\mathbf{A}}_i = \hat{\mathbf{A}}, \ \hat{\mathbf{B}}$ for $i = 1, 2$ respectively and

$$\Theta = k_x u + k_y v,$$

$$k_x = (\xi_i)_x, \quad i = 1, 2,$$

$$k_y = (\xi_i)_y, \quad i = 1, 2,$$

$$\xi_i = (\xi \ \text{ or } \ \eta) \text{ for } (\hat{\mathbf{A}} \ \text{ or } \ \hat{\mathbf{B}}).$$

A similarity transform for the Jacobian matrix is introduced by

$$\hat{\mathbf{A}}_i = \mathbf{R}_i \Lambda_i \mathbf{R}_i^{-1}, \tag{13}$$

with

$$\Lambda_i = \begin{bmatrix} \Theta & 0 & 0 \\ 0 & \Theta + c & 0 \\ 0 & 0 & \Theta - c \end{bmatrix}, \tag{14}$$

where c is the scaled artificial speed of sound given by

$$c = \sqrt{\Theta^2 + \beta(k_x^2 + k_y^2)}. \tag{15}$$

The matrix of the right eigenvectors is given by

$$\mathbf{R}_i = \frac{1}{2\beta c^2} \begin{bmatrix} 0 & \beta c & -\beta c \\ -2\beta k_y & u(\Theta + c) + \beta k_x & u(\Theta - c) + \beta k_x \\ 2\beta k_x & v(\Theta + c) + \beta k_y & v(\Theta - c) + \beta k_y \end{bmatrix} \tag{16}$$

and its inverse is given by

$$\mathbf{R}_i^{-1} = \begin{bmatrix} k_y u - k_x v & -v\Theta - \beta k_y & u\Theta + \beta k_x \\ c - \Theta & \beta k_x & \beta k_y \\ -c - \Theta & \beta k_x & \beta k_y \end{bmatrix}. \tag{17}$$

Now, we denote the sth right and left eigenvectors of $\mathbf{A}_{j+1/2}$ (the average Jacobian at $x_{j+1/2}$) by $\mathbf{r}_s$ (column vector) and $\mathbf{l}_s$ (row vector) respectively. Then the scalar WENO3 scheme can be applied to each of the characteristic fields, i.e.

$$\bar{\mathbf{F}}_{j+1/2,s} = \sum_{k=0}^{2} \omega_{k,s} q_k(\mathbf{l}_s \cdot \hat{\mathbf{F}}_{j+k-2}, \ldots, \mathbf{l}_s \cdot \hat{\mathbf{F}}_{j+k}), \tag{18}$$

which gives the numerical flux in the sth characteristic field. Here, $\omega_{k,s}$ $(k = 0, 1, 2)$ are the weights in the sth characteristic field,

$$\omega_{k,s} = \omega_k(\mathbf{l}_s \cdot \hat{\mathbf{F}}_{j-2}, \ldots, \mathbf{l}_s \cdot \hat{\mathbf{F}}_{j+2}), \tag{19}$$

which is a non-linear function, and q_k are the stencils as in Equations (10) and (11). The numerical fluxes obtained in each characteristic field can be projected back to the physical space by (here only the two-dimensional case is described)

$$\tilde{\mathbf{F}}_{j+1/2} = \sum_{s=1}^{3} \bar{\mathbf{F}}_{j+1/2,s} \mathbf{r}_s. \tag{20}$$

3.2. Time discretization

The lower–upper (LU) factored implicit scheme that was developed by Jameson and Yoon [22] is unconditionally stable in any number of space dimensions. In the framework of the LU implicit scheme, the flux vectors can be linearized by setting

$$
\begin{aligned}
\hat{\mathbf{E}}^{n+1} &= \hat{\mathbf{E}}^{n} + \hat{\mathbf{A}}^{n}\Delta\hat{\mathbf{Q}} + O(\|\Delta\hat{\mathbf{Q}}\|^2),\\
\hat{\mathbf{F}}^{n+1} &= \hat{\mathbf{F}}^{n} + \hat{\mathbf{B}}^{n}\Delta\hat{\mathbf{Q}} + O(\|\Delta\hat{\mathbf{Q}}\|^2),\\
\hat{\mathbf{E}}_v^{n+1} &= \hat{\mathbf{E}}_v^{n} + \hat{\mathbf{A}}_v^{n}\Delta\hat{\mathbf{Q}} + O(\|\Delta\hat{\mathbf{Q}}\|^2),\\
\hat{\mathbf{F}}_v^{n+1} &= \hat{\mathbf{F}}_v^{n} + \mathbf{B}_v^{n}\Delta\hat{\mathbf{Q}} + O(\|\Delta\hat{\mathbf{Q}}\|^2),
\end{aligned}
$$

where, n is the time level; $\hat{\mathbf{A}}$, $\hat{\mathbf{B}}$, $\hat{\mathbf{A}}_v$ and $\hat{\mathbf{B}}_v$ are the Jacobian matrices of the inviscid fluxes $\hat{\mathbf{E}}$, $\hat{\mathbf{F}}$ and the viscous fluxes $\hat{\mathbf{E}}_v$, $\hat{\mathbf{F}}_v$ respectively; and $\Delta\hat{\mathbf{Q}} = \hat{\mathbf{Q}}^{n+1} - \hat{\mathbf{Q}}^{n}$ is the increment or correction of conservative variables.

The inviscid Jacobians ($\hat{\mathbf{A}}_i = \hat{\mathbf{A}}, \hat{\mathbf{B}}$ for $i = 1, 2$ respectively) can be split according to the sign of eigenvalues,

$$\hat{\mathbf{A}}_i = \hat{\mathbf{A}}_i^{+} + \hat{\mathbf{A}}_i^{-} = \mathbf{R}_i\Lambda_i^{+}\mathbf{R}_i^{-1} + \mathbf{R}_i\Lambda_i^{-}\mathbf{R}_i^{-1}. \tag{21}$$

Here Λ_i^{+} is formed by the non-negative part of the Λ_i matrix and Λ_i^{-} by the non-positive part.

An unfactored implicit scheme can be obtained by substituting the above relations into Equation (4) and dropping terms of second- and higher-orders. This results in the governing equation in diagonally dominant form

$$
\begin{aligned}
&\frac{\mathbf{V}_{i,j}}{\Delta t}\mathbf{I}\Delta\hat{\mathbf{Q}}_{i,j} + \alpha\{[(\hat{\mathbf{A}}^{+} - \hat{\mathbf{A}}_v)\mathbf{S}]_{i+1/2,j}\Delta\hat{\mathbf{Q}}_{i,j} - [(\hat{\mathbf{A}}^{+} - \hat{\mathbf{A}}_v)\mathbf{S}]_{i-1/2,j}\Delta\hat{\mathbf{Q}}_{i-1,j}\\
&\quad + [(\hat{\mathbf{A}}^{-} + \hat{\mathbf{A}}_v)\mathbf{S}]_{i+1/2,j}\Delta\hat{\mathbf{Q}}_{i+1,j} - [(\hat{\mathbf{A}}^{-} + \hat{\mathbf{A}}_v)\mathbf{S}]_{i-1/2,j}\Delta\hat{\mathbf{Q}}_{i,j} + [(\hat{\mathbf{B}}^{+} - \hat{\mathbf{B}}_v)\mathbf{S}]_{i,j+1/2}\Delta\hat{\mathbf{Q}}_{i,j}\\
&\quad - [(\hat{\mathbf{B}}^{+} - \hat{\mathbf{B}}_v)\mathbf{S}]_{i,j-1/2}\Delta\hat{\mathbf{Q}}_{i,j-1} + [(\hat{\mathbf{B}}^{-} + \hat{\mathbf{B}}_v)\mathbf{S}]_{i,j+1/2}\Delta\hat{\mathbf{Q}}_{i,j+1} - [(\hat{\mathbf{B}}^{-} + \hat{\mathbf{B}}_v)\mathbf{S}]_{i,j-1/2}\Delta\hat{\mathbf{Q}}_{i,j}\}^{n}\\
&= -\{[(\hat{\mathbf{E}} - \hat{\mathbf{E}}_v)\mathbf{S}]_{i+1/2,j} - [(\hat{\mathbf{E}} - \hat{\mathbf{E}}_v)\mathbf{S}]_{i-1/2,j}\}^{n} - \{[(\hat{\mathbf{F}} - \hat{\mathbf{F}}_v)\mathbf{S}]_{i,j+1/2} - [(\hat{\mathbf{F}} - \hat{\mathbf{F}}_v)\mathbf{S}]_{i,j-1/2}\}^{n}\\
&\equiv \mathrm{RHS},
\end{aligned}
\tag{22}
$$

where $\mathbf{I}$ is the identity matrix. For $\alpha = \frac{1}{2}$, the scheme is second-order-accurate in time. For $\alpha = 1$, the time accuracy drops to first-order.

The implicit viscous Jacobian is also considered here to enhance the convergence rate, especially for high-Reynolds number flows in which high aspect ratio grids near the walls are used to resolve the boundary layer.

In order to maximize the efficiency, Jacobian matrices of the flux vectors are approximately constructed to give diagonal dominance. $\hat{\mathbf{A}}^{+}$, $\hat{\mathbf{A}}^{-}$, $\hat{\mathbf{B}}^{+}$ and $\hat{\mathbf{B}}^{-}$ are constructed so that the eigenvalues of '$+$' matrices are non-negative and those of '$-$' matrices are non-positive, i.e.

$$\hat{\mathbf{A}}_i^{\pm} = \frac{1}{2}[\hat{\mathbf{A}}_i \pm \rho_{\hat{\mathbf{A}}_i}\mathbf{I}], \tag{23}$$

with the spectral radius of Jacobians

$$\rho_{\hat{\mathbf{A}}_i} = \kappa \max[|\lambda(\hat{\mathbf{A}}_i)|], \tag{24}$$

where $\lambda(\hat{\mathbf{A}}_i)$ represent eigenvalues of the Jacobian matrix $\hat{\mathbf{A}}_i$ and κ is a constant that is greater than or equal to 1 to ensure the splitting of flux Jacobians is diagonally dominant.

Equation (22) can be simplified if all of the Jacobians that should be evaluated at the indicated cell faces are calculated at the local cell centers, and this can be achieved if two-point one-sided differences are used. In addition, if it is assumed that the adjacent cell faces on the diagonal are approximately equal, say in i-direction,

$$\mathbf{S}_{i+1/2,j} \simeq \mathbf{S}_{i-1/2,j} = \mathbf{S}_I = 0.5(\mathbf{S}_{i+1/2,j} + \mathbf{S}_{i-1/2,j}), \tag{25}$$

and recognize that

$$\hat{\mathbf{A}}^+ - \hat{\mathbf{A}}^- = \rho_{\hat{\mathbf{A}}}, \tag{26}$$

and replace all viscous Jacobians with their spectral radius approximation then

$$\hat{\mathbf{A}}_v \simeq \rho_{\hat{\mathbf{A}}_v} = \frac{vS_I}{\mathbf{V}}\mathbf{I}. \tag{27}$$

The unfactored implicit scheme, Equation (22), produces a large block banded matrix that is very costly to invert and requires large amounts of storage. This difficulty can be solved by adopting the LU factored implicit scheme. In this paper, the LU symmetric successive overrelaxation (LU-SSOR) scheme of Yoon and Jameson [21] is adopted to solve the unsteady flow problems. The LU-SSOR implicit factorization scheme has the advantages of LU factorization and SSOR relaxation. Using the above relations, the LU-SSOR scheme can be written as

$$[\mathbf{L}\mathbf{N}^{-1}\mathbf{U}]^n \Delta\hat{\mathbf{Q}} = \mathrm{RHS}^n, \tag{28}$$

where

$$\begin{aligned}
\mathbf{L} &= \frac{\mathbf{V}_{i,j}}{\Delta t}\mathbf{I} + \alpha\{[(\rho_{\hat{\mathbf{A}}} + 2\rho_{\hat{\mathbf{A}}_v})\mathbf{S}_I + (\rho_{\hat{\mathbf{B}}} + 2\rho_{\hat{\mathbf{B}}_v})S_J]_{i,j} \\
&\quad - [(\hat{\mathbf{A}}^+ + \rho_{\hat{\mathbf{A}}_v})_{i-1,j}\mathbf{S}_{i-1/2,j} + (\hat{\mathbf{B}}^+ + \rho_{\hat{\mathbf{B}}_v})_{i,j-1}\mathbf{S}_{i,j-1/2}]\}, \\
\mathbf{N} &= \frac{\mathbf{V}_{i,j}}{\Delta t}\mathbf{I} + \alpha[(\rho_{\hat{\mathbf{A}}} + 2\rho_{\hat{\mathbf{A}}_v})\mathbf{S}_I + (\rho_{\hat{\mathbf{B}}} + 2\rho_{\hat{\mathbf{B}}_v})\mathbf{S}_J]_{i,j}, \\
\mathbf{U} &= \frac{\mathbf{V}_{i,j}}{\Delta t}\mathbf{I} + \alpha\{[(\rho_{\hat{\mathbf{A}}} + 2\rho_{\hat{\mathbf{A}}_v})\mathbf{S}_I + (\rho_{\hat{\mathbf{B}}} + 2\rho_{\hat{\mathbf{B}}_v})\mathbf{S}_J]_{i,j} \\
&\quad + [(\hat{\mathbf{A}}^- - \rho_{\hat{\mathbf{A}}_v})_{i+1,j}\mathbf{S}_{i+1/2,j} + (\hat{\mathbf{B}}^- - \rho_{\hat{\mathbf{B}}_v})_{i,j+1}\mathbf{S}_{i,j+1/2}]\}.
\end{aligned} \tag{29}$$

By setting $\alpha = 1$, the scheme reduces to a Newton iteration in the limit $\Delta t \to \infty$. Then, Equation (29) reduces to

$$\begin{aligned}
\mathbf{L} &= [(\rho_{\hat{\mathbf{A}}} + 2\rho_{\hat{\mathbf{A}}_v})\mathbf{S}_I + (\rho_{\hat{\mathbf{B}}} + 2\rho_{\hat{\mathbf{B}}_v})\mathbf{S}_J]_{i,j} \\
&\quad - [(\hat{\mathbf{A}}^+ + \rho_{\hat{\mathbf{A}}_v})_{i-1,j}\mathbf{S}_{i-1/2,j} + (\hat{\mathbf{B}}^+ + \rho_{\hat{\mathbf{B}}_v})_{i,j-1}\mathbf{S}_{i,j-1/2}], \\
\mathbf{N} &= [(\rho_{\hat{\mathbf{A}}} + 2\rho_{\hat{\mathbf{A}}_v})\mathbf{S}_I + (\rho_{\hat{\mathbf{B}}} + 2\rho_{\hat{\mathbf{B}}_v})\mathbf{S}_J]_{i,j}, \\
\mathbf{U} &= [(\rho_{\hat{\mathbf{A}}} + 2\rho_{\hat{\mathbf{A}}_v})\mathbf{S}_I + (\rho_{\hat{\mathbf{B}}} + 2\rho_{\hat{\mathbf{B}}_v})S_J]_{i,j} \\
&\quad + [(\hat{\mathbf{A}}^- - \rho_{\hat{\mathbf{A}}_v})_{i+1,j}\mathbf{S}_{i+1/2,j} + (\hat{\mathbf{B}}^- - \rho_{\hat{\mathbf{B}}_v})_{i,j+1}\mathbf{S}_{i,j+1/2}].
\end{aligned} \tag{30}$$

It is interesting to note that the present implicit algorithm (LU-SGS) eliminates the need for block inversions and is completely vectorizable on $i + j = \text{constant}$ oblique planes of sweep.

3.3. Boundary conditions

The boundary conditions imposed on the solid surface are the no-slip condition for viscous flows and the tangency condition for inviscid flows. A zero normal pressure gradient on the wall is applied. In the far-field, a locally one-dimensional characteristic-type of boundary condition is used. The procedures employed here are similar to those usually used for the compressible flows. The Riemann invariants for this system of equations are now given by

$$\mathbf{R}^{\pm} = p + \frac{1}{2} u_n^2 \pm \frac{1}{2} [u_n c + \beta \ln(u_n + c)], \tag{31}$$

where u_n is the component of the velocity normal to the boundary. In all calculations, the above boundary conditions are treated explicitly.

4. RESULTS AND DISCUSSION

Presented in this section are the results of four different laminar flow computations. For the steady cases, these are driven cavity flow and flow over a backward-facing step. For the unsteady cases, these are flow decayed by viscosity and flow over a circular cylinder.

4.1. Driven cavity flow

The first problem considered here is the two-dimensional lid-driven square cavity flow, which has been adopted as a benchmark for code validation of two-dimensional incompressible Navier–Stokes equations for decades.

The flow fields with Reynolds number 100, 400, 1000 and 3200 have been calculated using a 65 × 65 grid system that is clustered near walls. Figure 1 shows the geometry and the boundary conditions for the flow in a driven cavity. In Figure 2, the computed u velocity along vertical lines and v velocity along horizontal lines through the geometric center are shown, and numerical solutions by Ghia *et al.* [23] using a 129 × 129 uniform fine grid system are also given for comparison. Excellent agreement can be observed, even with the current coarse grid.

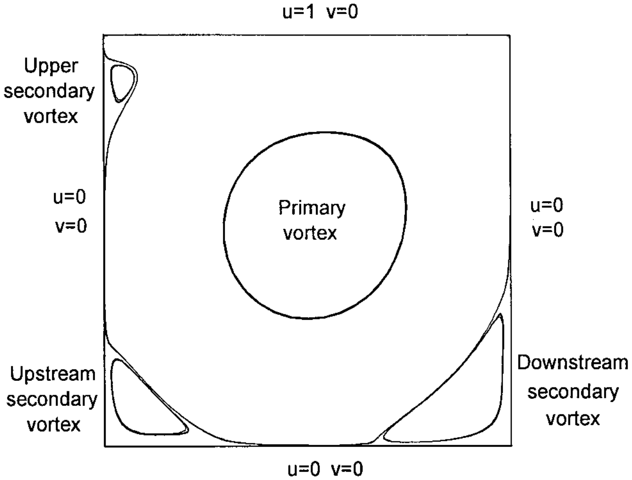

Figure 1. The geometry and boundary conditions for the driven square cavity flow.

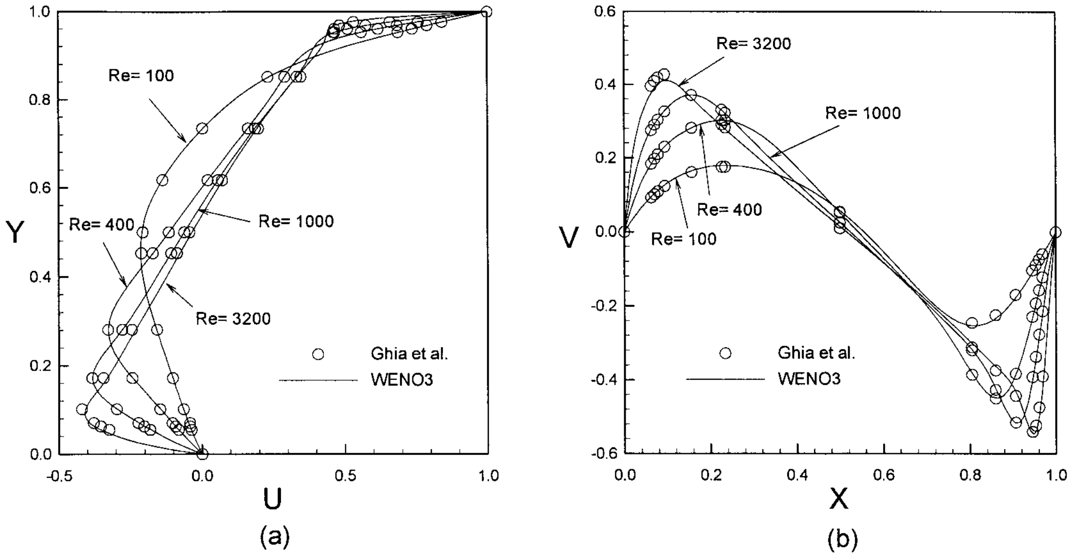

Figure 2. (a) u velocity component along vertical centerline, (b) v velocity component along horizontal centerline for the cavity flow.

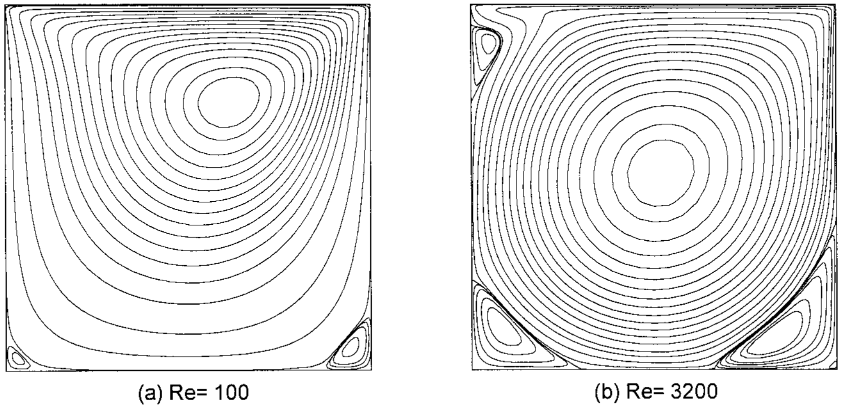
(a) Re= 100
(b) Re= 3200

Figure 3. Streamline patterns for the cavity flow.

Figure 3 shows the streamline patterns for $Re = 100$ and 3200. It can be seen that the center of the primary vortex is offset towards the top right corner at $Re = 100$. It moves towards the geometric center of the cavity with increasing Reynolds number. The solutions of the present scheme show very good agreement with the benchmark solutions obtained by Ghia *et al.* [23].

The effect of various artificial compressibility parameters, β, on the convergence history is shown in Figure 4. The parameter β is a measure for the amount of artificial compressibility. For very large β, the modified governing equations resemble the Navier–Stokes equations for truly incompressible flow. In Figure 4, as β is increased, the governing equations become more stiff and the convergence rate becomes slow. As β is decreased, the convergence rate is better. However, for very small β, the upstream influence of a local pressure disturbance is nearly lost, which could cause numerical divergence (e.g. $\beta = 0.1$). In general, for steady state flow problems, β is set to unity. When a steady state solution is approached, the effect of artificial compressibility diminishes, resulting in an incompressible solution.

Figure 5 shows the convergence rates of the ENO scheme ($r = 2$) [24] and the WENO scheme ($r = 3$) for the cavity flow at $Re = 100$ and $\beta = 1$. The convergence rate of the WENO is obviously more superior to that of the ENO scheme.

4.2. *Flow over a backward-facing step*

Next we consider the flow over a backward-facing step. The geometry and boundary conditions for this flow are shown in Figure 6. A parabolic velocity profile is prescribed at the inlet, whereas Neumann-type conditions (zero normal derivatives for both velocity components) are imposed at the outlet of the computational domain. All the results presented are

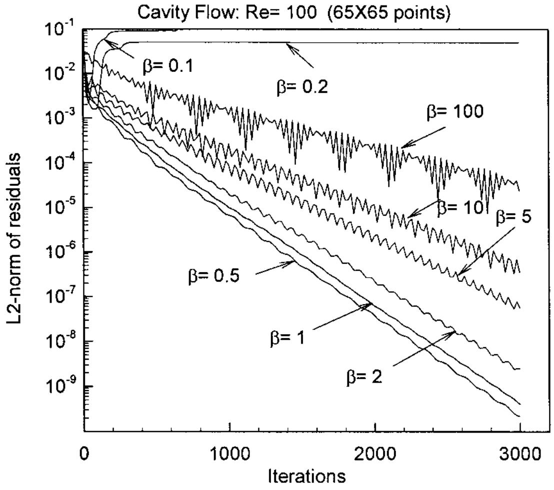

Figure 4. The effect of artificial compressibility parameters β on the convergence history.

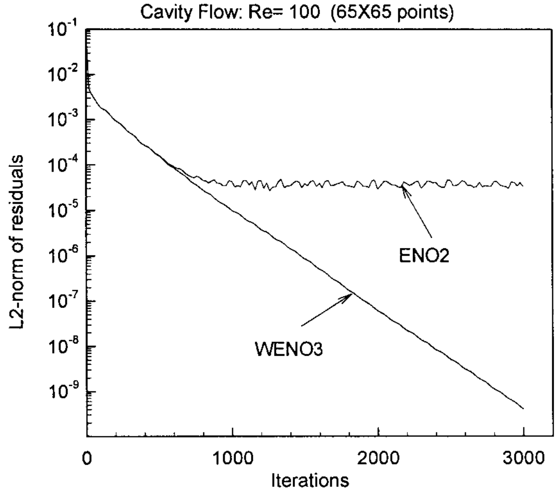

Figure 5. The convergence rate of ENO and WENO schemes for the cavity flow at Reynolds number 100 and $\beta = 1$.

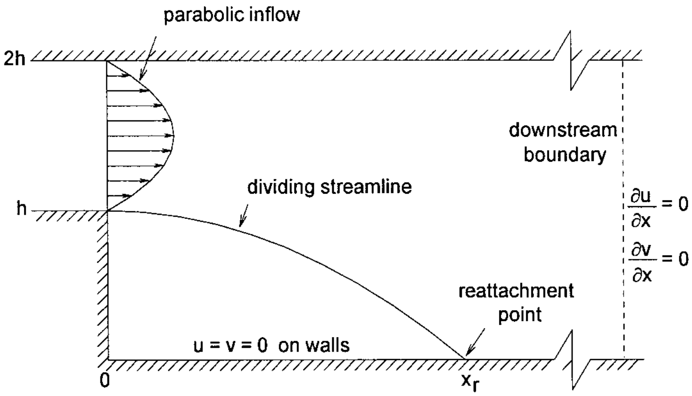

Figure 6. The geometry and boundary conditions for the flow over a backward-facing step.

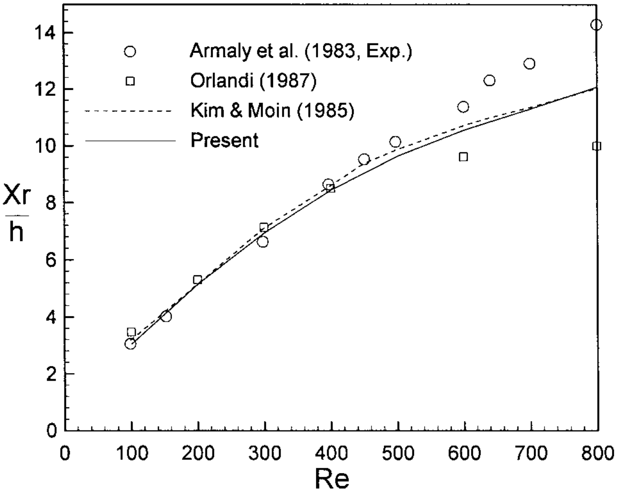

Figure 7. Reattachment length as a function of Reynolds number.

obtained using 101 × 101 grid points and the downstream boundary was located at 30 step heights, as in Kim and Moin [25].

In Figure 7, numerical results for different Reynolds numbers are shown and compared with the experimental and computational results of Armaly *et al.* [26] and the computational results of Orlandi [27] and of Kim and Moin [25]. The present calculation shows good agreement with experimental results up to $Re = 400$. At this Reynolds number the corresponding velocity vectors and streamlines are shown in Figure 8. As the Reynolds number become larger than 400, the computed results start to deviate from the experimental values. As Armaly *et al.* [26] have pointed out, the difference is due to the three-dimensionality of the experimental flow at this Reynolds number. In comparison with the numerical results of Armaly *et al.* [26] (using the TEACH code), Orlandi [27] (using the vorticity–velocity formulation) and Kim and Moin (using the fractional step method), the present results show a much higher reattachment length than those of Armaly *et al.* [26] and Orlandi [27], and is approximately the same as that of Kim and Moin.

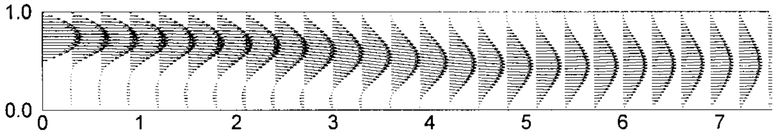

(a) velocity vectors

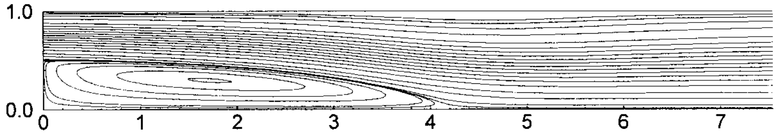

(b) streamlines

Figure 8. The velocity vectors and streamlines for the backward-facing step flow at $Re = 400$.

4.3. *Flow decayed by viscosity*

This example is chosen to check the implicit fifth-order accuracy of WENO schemes (WENO3) for the unsteady smooth solutions. The initial condition is taken as

$$u(x, y, 0) = -\cos(x)\sin(y),$$
$$v(x, y, 0) = \sin(x)\cos(y), \tag{32}$$

which was used in Reference [28]. The exact solution for this case is known

$$u(x, y, t) = -\cos(x)\sin(y)\,\mathrm{e}^{-2\mu t},$$
$$v(x, y, t) = \sin(x)\cos(y)\,\mathrm{e}^{-2\mu t}. \tag{33}$$

In the present paper, μ is taken as 0.05 (i.e. the corresponding Reynolds number is 20) and the computational domain is defined on the box $[0, 2\pi] \times [0, 2\pi]$ with periodic boundary conditions in both directions. Since the u velocity along vertical lines and the v velocity along horizontal lines through the geometric center are symmetric and have the same maximum amplitude, we take the maximum velocity and define a percentage error as

$$\text{Percentage error} = \left|\frac{u_{\text{exact}} - u_{\text{calculated}}}{u_{\text{exact}}}\right| \times 100\%.$$

Table I shows the calculated percentage errors for different artificial compressibility parameters β and grid systems. Since each case is calculated with the same CFL number, this implies that the calculating time steps are increased as β is increased. For the consideration of both accuracy and CPU time, the current recommended range of β values for unsteady flow problems is $5 \leq \beta \leq 100$. Figures 9 and 10 show the comparison of the calculated u velocity along vertical lines and the v velocity along horizontal lines through the geometric center with exact solutions. The calculated results ($\beta = 10$) are in very good agreement with exact

Table I. The percentage error of maximum velocity at $t = 10$

β	1	5	10	100	1000
Grid: 65×65	5.463%	1.443%	0.655%	0.233%	0.206%
Grid: 129×129	5.211%	1.220%	0.533%	0.038%	0.112%

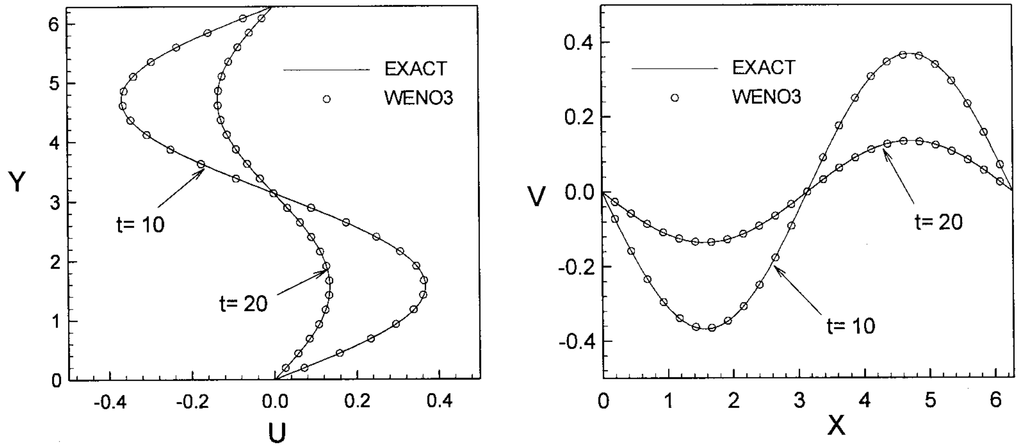

Figure 9. The u velocity component along vertical centerline and the v velocity component along horizontal centerline for the flow decayed by viscosity at 129 × 129 grid points.

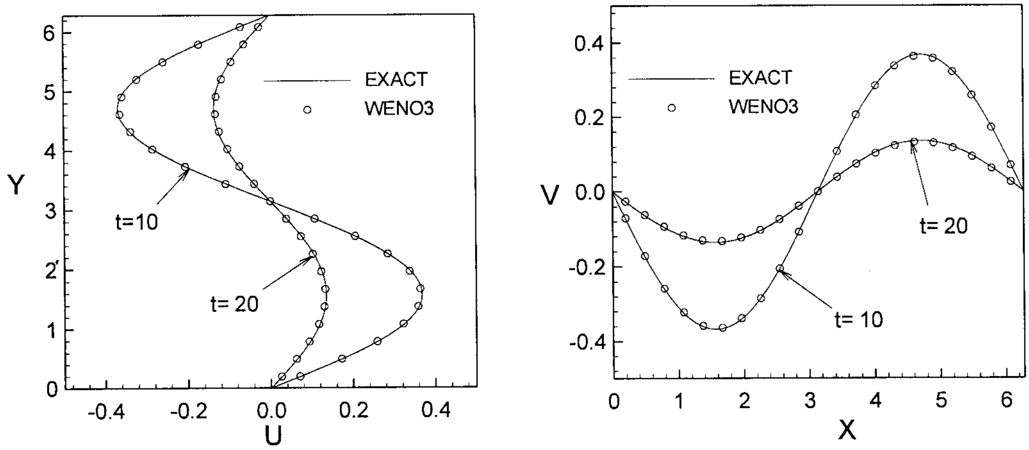

Figure 10. The u velocity component along vertical centerline and the v velocity component along horizontal centerline for the flow decayed by viscosity at 65 × 65 grid points.

solutions. In this case, without using the pseudo-time iteration approach, one can predict the time-dependent flow problem very well.

4.4. *Flow over a circular cylinder*

The two-dimensional flow over a circular cylinder is solved as an example of an external flow over a bluff body with a complicated flow field that strongly depends on the Reynolds number. For $6 < Re < 40$, a steady state exists with a pair of symmetric separation bubbles on the leeward side. At higher Reynolds numbers the flow field is inherently unsteady and is characterized by vortex shedding.

In this paper, the flow over a circular cylinder was computed for Reynolds number $Re = 40$ and $Re = 200$ (based on the diameter). No-slip boundary conditions were specified on the cylinder and characteristic boundary conditions were used to treat the far-field.

For the case of $Re = 40$, an O-grid system of 181×65, with the first grid spacing of 0.005 diameters and stretching to the outer boundary with 20 diameters, is taken. Three values of β (5, 10 and 50) under this grid system were tested. In this case the time step is determined by $\mathrm{CFL} = 0.5$ for each different Reynolds number. In Figure 11, the time evolution of the separation length (measured from the rear of the cylinder and normalized by the diameter) for three different values of β are compared with the experimental results of Coutanceau and Bouard [29]. The results show good agreement with the experimental data. The corresponding streamlines for $\beta = 10$ (it seems to give the best agreement with the experimental results) are shown in Figure 12.

For the case of $Re = 200$, an O–H-grid system of 91×65 O-grids, with the first grid spacing of 0.005 diameters and stretching to the outer boundary with 5 diameters, combining with a 121×39 H-grid extended 15 diameters to the downstream is taken. The grid system is shown in Figure 13. This case was done having $\beta = 10$ and $\mathrm{CFL} = 0.8$ (the corresponding time step is approximately 0.001) under the grid system. The lift and drag coefficients are plotted versus time in Figure 14. A comparison of the calculated results of the present work with the experimental results (Wille [30] and Roshko [31]) and other calculations (Rogers and Kwak [32], Rosenfeld *et al.* [33] and Lecointe and Piquet [34]) is listed in Table II. The lift and drag coefficients for the periodic state and the corresponding Strouhal number appear to be quite consistent with the experimental results. In Figure 15, the streamlines at various stages during one period are plotted. The first plot shows the flow when the drag is at a minimum and the lift is zero. The second plot shows that the flow has a maximum in drag and lift. The next two plots correspond to another minimum in drag with zero lift, and a maximum in drag with a

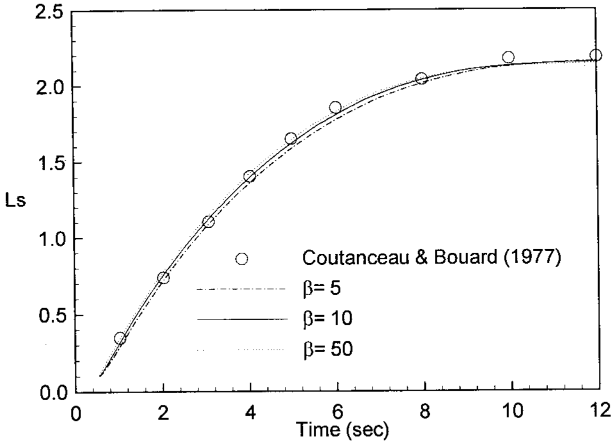

Figure 11. Time evolution of separation length for flow over a circular cylinder at $Re = 40$.

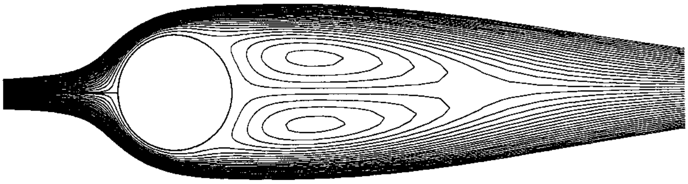

Figure 12. The streamlines for flow over a circular cylinder at $Re = 40$.

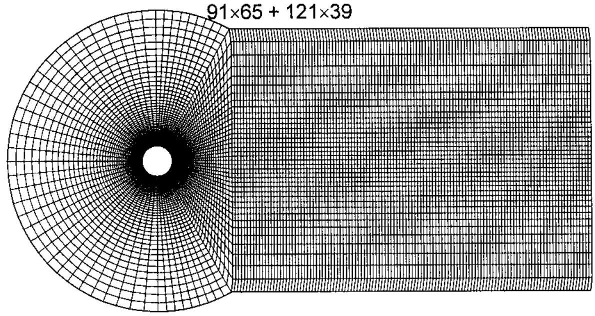

Figure 13. The computational grid system for flow over a circular cylinder at $Re = 200$.

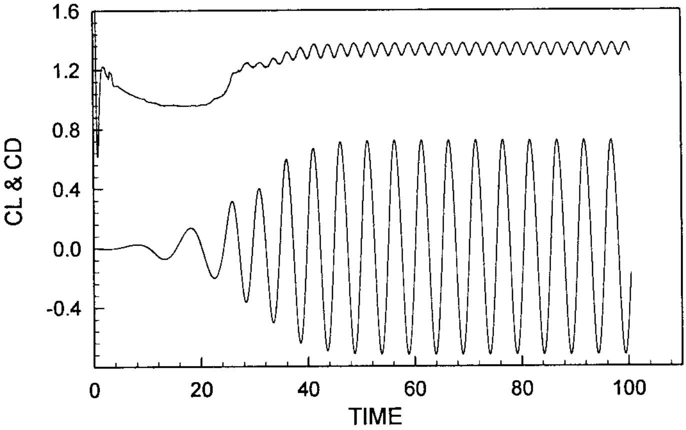

Figure 14. Lift and drag coefficients vs. time for flow over a circular cylinder at $Re = 200$.

Table II. Lift and drag coefficients and Strouhal numbers for circular cylinder flow at $Re = 200$

		C_D	C_L	St
Present		1.33 ± 0.04	± 0.72	0.197
Rogers and Kwak [32]	third-order	1.29 ± 0.05	± 0.75	0.160
	fifth-order	1.23 ± 0.05	± 0.65	0.185
Rosenfeld *et al.* [33]		1.40 ± 0.04	± 0.70	0.201
Lecointe and Piquet [34]	second-order	1.46 ± 0.04	± 0.70	0.227
	fourth-order	1.58 ± 0.0035	± 0.50	0.194
Wille (experimental) [30]		1.3		
Roshko (experimental) [31]				0.19

minimum in lift respectively. These two are mirror images of the first two plots. Finally, the last plot is identical to the first one, and the period for this flow is 5.072 (i.e. the corresponding Strouhal number is 0.197). To show the vortex shedding phenomenon, the pressure contours and streamlines covering the whole computational domain are shown in Figure 16.

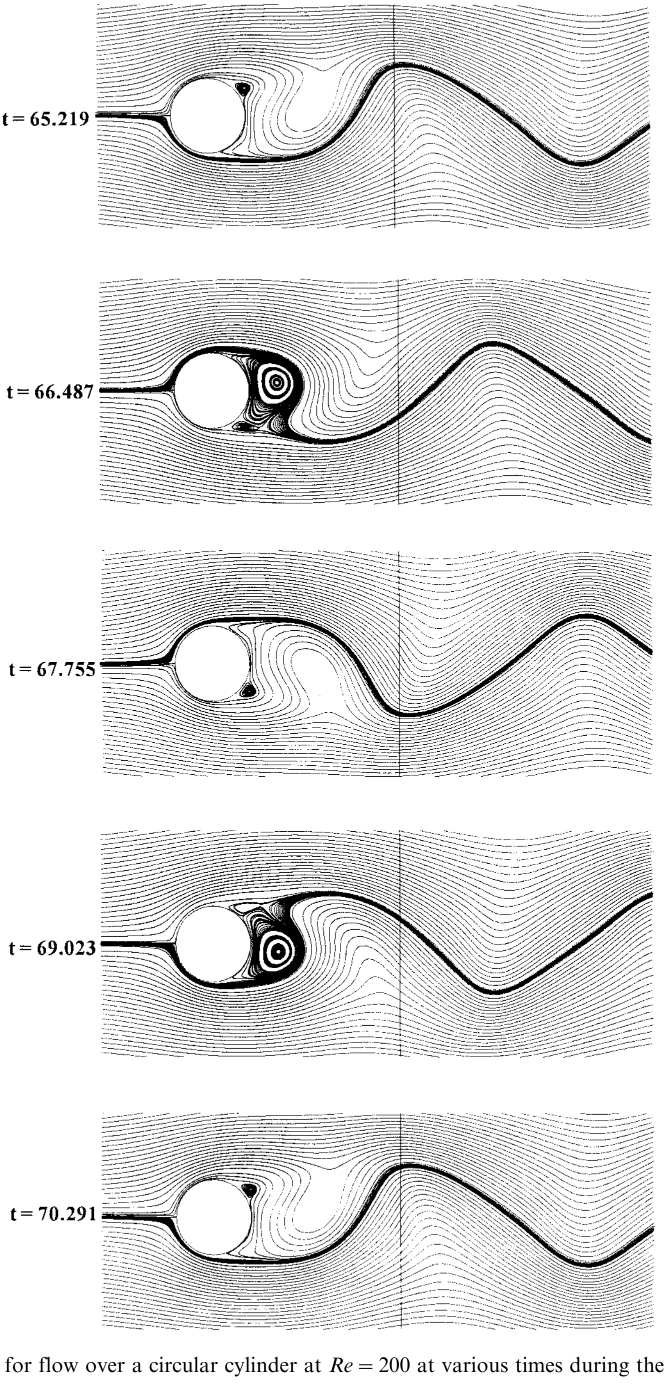

Figure 15. Streamlines for flow over a circular cylinder at $Re = 200$ at various times during the vortex shedding cycle.

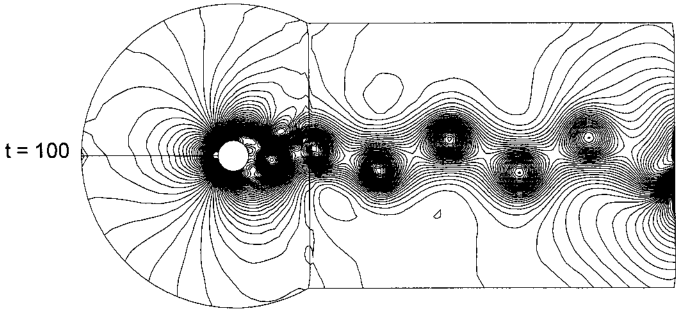

(a) pressure contours

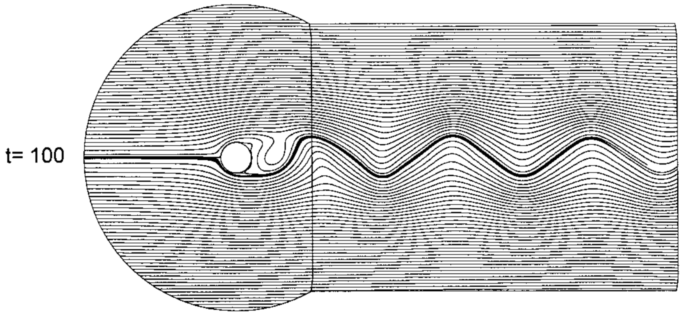

(b) streamlines

Figure 16. (a) Pressure contours and (b) streamlines for flow over a circular cylinder at $Re = 200$.

5. CONCLUSIONS

An accurate and efficient incompressible Navier–Stokes code based on the artificial compressibility formulation of Chorin [6] has been developed. This code uses the implicit LU-SGS [20] and LU-SSOR [21] time stepping and extends the WENO spatial operator of Jiang and Shu [4] to the case of incompressible flows. Applications to several two-dimensional steady and unsteady viscous incompressible flow problems have been carried out to validate and illustrate the code. For steady flow problems, the lid-driven cavity flow and flow over a backward-facing step, the LU-SGS implicit algorithm is used. For time-dependent flow problems, flow decayed by viscosity and flow over a circular cylinder, the LU-SSOR scheme is employed. The use of the WENO spatial operator for the inviscid fluxes not only enhances the accuracy but also improves the convergence rate for the steady state computation as compared with using the ENO counterpart. It is found that the solutions of the present algorithm compare well with exact solutions, experimental data and other numerical results. Extending the present method to three space dimensions can be done and is currently being developed.

ACKNOWLEDGMENTS

The authors wish to thank the referees for many valuable comments. This work was sponsored by the National Science Council, ROC, through Grant NSC 84-0210-D002-019. Dr Wun-Wen Lin of Chung-Shan Institute of Science and Technology is the technical monitor.

REFERENCES

1. A. Harten, B. Engquist, S. Osher and S. Chakravarthy, ‘Uniformly high-order accurate nonoscillatory schemes’, *J. Comput. Phys.*, **71**, 231–303 (1987).
2. C.-W. Shu and S. Osher, ‘Efficient implementation of nonoscillatory shock capturing schemes’, *J. Comput. Phys.*, **77**, 439–471 (1988).
3. C.-W. Shu and S. Osher, ‘Efficient implementation of nonoscillatory shock capturing schemes, II’, *J. Comput. Phys.*, **83**, 32–78 (1988).
4. G.S. Jiang and C.-W. Shu, ‘Efficient implementation of weighted ENO schemes’, *J. Comput. Phys.*, **126**, 202–228 (1996).
5. X.-D. Liu, S. Osher and T. Chan, ‘Weighted essentially nonoscillatory schemes’, *J. Comput. Phys.*, **115**, 200–212 (1994).
6. A.J. Chorin, ‘A numerical method for solving incompressible viscous flow problems’, *J. Comput. Phys.*, **2**, 12–26 (1967).
7. R.M. Beam and R.F. Warming, ‘An implicit factored scheme for the compressible Navier–Stokes equations’, *AIAA J.*, **16**, 393–402 (1978).
8. J.L. Steger and P. Kutler, ‘Implicit finite difference procedures for the computation of vortex wakes’, *AIAA J.*, **15**, 581–590 (1977).
9. D. Choi and C.L. Merkle, ‘Application of time-iterative schemes to incompressible flow’, *AIAA J.*, **23**, 1518–1524 (1985).
10. D. Kwak, J.L.C. Chang, S.P. Shanks and S.R. Chakravarthy, ‘A three-dimensional incompressible Navier–Stokes flow solver using primitive variables’, *AIAA J.*, **24**, 390–396 (1986).
11. J.L.C. Chang, D. Kwak and S.C. Dao, ‘A three-dimensional incompressible flow simulation method and its application to the space shuttle main engine. Part I. Laminar flow’, *AIAA Paper 85-0175*, 1985.
12. J.L.C. Chang, D. Kwak, S.C. Dao and R. Rosen, ‘A three-dimensional incompressible flow simulation method and its application to the space shuttle main engine. Part II. Turbulent flow’, *AIAA Paper 85-1670*, 1985.
13. J.L.C. Chang and D. Kwak, ‘Numerical study of turbulent internal shear layer flow in an axisymmetric U-duct’, *AIAA Paper 88-0596*, 1988.
14. J.L.C. Chang, D. Kwak, S.E. Rogers and R.J. Yang, ‘Numerical simulation methods of incompressible flows and an application to the space shuttle main engine’, *Int. J. Numer. Methods Fluids*, **8**, 1241–1268 (1988).
15. C.L. Merkle and M. Athavale, ‘Time-accurate unsteady incompressible flow algorithms based on artificial compressibility’, *AIAA Paper 87-1137*, 1987.
16. S.E. Rogers and D. Kwak, ‘An upwind differencing scheme for the time-accurate incompressible Navier–Stokes equations’, *AIAA Paper 88-2583*, 1988.
17. S.E. Rogers, D. Kwak and C. Kiris, ‘Numerical solution of the incompressible Navier–Stokes equations for steady state and time-dependent problems’, *AIAA Paper 89-0463*, 1989.
18. W.K. Anderson, R.D. Rausch and D.L. Bonhaus, ‘Implicit/multigrid algorithms for incompressible turbulent flows on unstructured grids’, *AIAA-95-1740-CP*, 1995.
19. W.R. Briley, S.S. Neerarambam and D.L. Whitfield, ‘Implicit lower–upper/approximate-factorization algorithms for viscous incompressible flows’, *AIAA-95-l742-CP*, 1995.
20. S. Yoon, D. Kwak and L. Chang, ‘LU-SGS implicit algorithm for three-dimensional incompressible Navier–Stokes equations with source term’, *AIAA Paper 89-196l-CP*, 1989.
21. S. Yoon and A. Jameson, ‘An LU-SSOR scheme for the Euler and Navier–Stokes equaions’, *AIAA Paper 87-0600*, 1987.
22. A. Jameson and S. Yoon, ‘Lower–upper implicit schemes with multiple grids for the Euler equations’, *AIAA J.*, **25**, 929–935 (1987).
23. U. Ghia, K.N. Ghia and C.T. Shin, ‘High-*Re* solutions for incompressible flow using the Navier–Stokes equations and a multigrid method’, *J. Comput. Phys.*, **48**, 387–411 (1982).
24. J.Y. Yang and C.A. Hsu, ‘High-resolution, nonoscillatory schemes for unsteady compressible flows’, *AIAA J.*, **30**, 1570–1575 (1992).
25. J. Kim and P. Moin, ‘Application of a fractional-step method to incompressible Navier–Stokes equations’, *J. Comput. Phys.*, **59**, 308–323 (1985).
26. B.F. Armaly, F. Durst, J.C.F. Pereira and B. Schonung, ‘Experimental and theoretical investigation of backward-facing step flow’, *J. Fluid Mech.*, **127**, 473–496 (1983).
27. P. Orlandi, ‘Vorticity–velocity formulation for high *Re* flows’, *Comput. Fluids*, **15**, 137–149 (1987).
28. A.J. Chorin, ‘Numerical solution of Navier–Stokes equations’, *Math. Comput.*, **22**, 740–762 (1968).
29. M. Coutanceau and R. Bouard, ‘Experimental determination of the main features of the viscous flow in the wake of a circular cylinder in uniform translation. Part 2. Unsteady flow’, *J. Fluid Mech.*, **79**, 257–272 (1977).
30. R. Wille, ‘Karman vortex streets’, *Adv. Appl. Mech.*, **6**, 273 (1960).
31. A. Roshko, ‘On the development of turbulent wakes from vortex streets’, *NACA Report 1191*, 1954.
32. S.E. Rogers and D. Kwak, ‘An upwind differencing scheme for the time-accurate incompressible Navier–Stokes equations’, *AIAA Paper 88-2583*, 1988.
33. M. Rosenfeld, D. Kwak and M. Vinokur, ‘A solution method for the unsteady and incompressible Navier–Stokes equations in generalized coordinate systems’, *AIAA Paper 88-0718*, 1988.
34. Y. Lecointe and J. Piquet, ‘On the use of several compact methods for the study of unsteady incompressible viscous flow round a circular cylinder’, *Comput. Fluids*, **12**, 255–280 (1984).